Materials Science and Engineering A 529 (2011) 311–320

Contents lists available at SciVerse ScienceDirect

Materials Science and Engineering A

journal homepage: www.elsevier.com/locate/msea

Microstructure and properties of a refractory $NbCrMo_{0.5}Ta_{0.5}TiZr$ alloy

O.N. Senkov[a,b,*], C.F. Woodward[a]

[a] Air Force Research Laboratory, Materials and Manufacturing Directorate, Wright-Patterson Air Force Base, OH 45433, USA
[b] UES Inc., Dayton, OH 45432, USA

ARTICLE INFO

Article history:
Received 3 June 2011
Received in revised form 25 August 2011
Accepted 9 September 2011
Available online 16 September 2011

Keywords:
Alloy design
High entropy alloy
Crystallography
Microstructure
Mechanical properties

ABSTRACT

A new refractory alloy, $Nb_{20}Cr_{20}Mo_{10}Ta_{10}Ti_{20}Zr_{20}$, was produced by vacuum arc melting. To close shrinkage porosity, it was hot isostatically pressed (HIPd) at $T = 1723$ K and $P = 207$ MPa for 3 h. In both as-solidified and HIPd conditions, the alloy contained three phases: two body centered cubic (BCC1 and BCC2) and one face centered cubic (FCC). The BCC1 phase was enriched with Nb, Mo and Ta and depleted with Zr and Cr, and its lattice parameter after HIP was $a = 324.76 \pm 0.16$ pm. The BCC2 phase was enriched with Zr and Ti and considerably depleted with Mo, Cr and Ta, and its lattice parameter after HIP was estimated to be $a = 341.0 \pm 1.0$ pm. The FCC phase was highly enriched with Cr and it was identified as a Laves C15 phase, $(Zr,Ta)(Cr,Mo,Nb)_2$, with the lattice parameter $a = 733.38 \pm 0.18$ pm. The volume fractions of the BCC1, BCC2 and FCC phases were 67%, 16% and 17%, respectively. The alloy density and Vickers microhardness were $\rho = 8.23 \pm 0.01$ g/cm^3 and $H_v = 5288 \pm 71$ MPa. The alloy had compression yield strength of 1595 MPa at 296 K, 983 MPa at 1073 K, 546 MPa at 1273 K and 171 MPa at 1473 K. During deformation at 296 K and 1073 K, the alloy showed a mixture of ductile and brittle fracture after plastic compression strain of ~5–6%. No macroscopic fracture was observed after 50% compression strain at 1273 K and 1473 K. Phase transformations and particle coarsening considerably accelerated by the plastic deformation occurred in the temperature range of 1073–1473 K.

1. Introduction

Metallic alloys with superior mechanical properties at elevated temperatures and low density remain in high demand for the aerospace industry. For example, the specific core power of a high pressure turbine engine is known to increase with an increase in the turbine rotor inlet temperature and significant turbine engine efficiencies can be achieved by running at higher temperatures [1]. These applications have benefited from decades of development of nickel-based (Ni) superalloys, which have allowed a steady increase in operating temperatures and led to improved performance and efficiency [2]. Currently, Ni-based superalloys have the best combination of required elevated temperature properties, such as creep resistance, temperature capability, environmental resistance, and damage tolerance, among all other known alloys. However, operating temperatures are reaching the theoretical limits of these materials, whose incipient melting temperatures are in the range of 1440–1540 K, depending on the composition. Engineering solutions to this materials problem require active or passive cooling thus increasing parasitic weight and decreasing overall flight efficiency and capability (maneuverability, fuel consumption, etc.) of supersonic/hypersonic vehicles. New metallic materials with higher melting points, such as refractory molybdenum (Mo) and niobium (Nb) alloys, are now being seriously examined as alternatives by academic and industrial groups [3–5].

The refractory metals and alloys, a group of metallic materials with melting points above 2123 K, are creep resistant at temperatures above 1073 K. High temperature strength and creep resistance are the key properties of these alloys, since considerable alloy softening generally occurs at temperatures above ~0.5–0.6 T_m, where T_m is the absolute melting temperature. At the same time, poor low-temperature ductility, poor oxidation resistance at high temperatures and high density limit the range of applications of many refractory alloys.

In recent publications [6–9] a new, so-called high entropy alloying (HEA) approach, invented by Yeh et al. [10–12], was used to develop new refractory alloys, which contain several principal alloying elements at near equiatomic concentrations. These are $Ta_{25}Nb_{25}W_{25}Mo_{25}$, $Ta_{20}Nb_{20}W_{20}Mo_{20}V_{20}$ [6,7] and $Ta_{20}Nb_{20}Hf_{20}Zr_{20}Ti_{20}$ [8,9]. All three alloys had a single-phase BCC crystal structure. The two alloys containing W, retained extremely high strength at temperatures at least up to 1873 K; however, they were brittle at room temperature. At the same time, the $Ta_{20}Nb_{20}Hf_{20}Zr_{20}Ti_{20}$ alloy showed high strength and very good ductility at room temperature [8], however, the strength of this

* Corresponding author at: UES Inc., 4401 Dayton-Xenia Rd., Dayton, OH 45432-1894, USA. Tel.: +1 937 255 4064; fax: +1 937 656 7292.
E-mail address: oleg.senkov@wpafb.af.mil (O.N. Senkov).

0921-5093/$ – see front matter © 2011 Elsevier B.V. All rights reserved.
doi:10.1016/j.msea.2011.09.033

Table 1
Chemical composition of the $NbCrMo_{0.5}Ta_{0.5}TiZr$ alloy produced by vacuum arc melting.

Composition	Nb	Cr	Mo	Ta	Ti	Zr
At.%	21.84	18.39	10.04	11.86	19.40	18.48
Wt.%	23.30	10.98	11.06	24.64	10.67	19.36

alloy rapidly decreased to below 100 MPa at temperatures above 1473 K and cavitation occurred during deformation at $T \sim 1073$ K and strain rates above 10^{-3} s^{-1} [9]. Among these three alloys, the $Ta_{20}Nb_{20}Hf_{20}Zr_{20}Ti_{20}$ alloy had the lowest density of 9.8 g/cm^3. In the present paper, we report on a new lower density refractory alloy, $Nb_{20}Cr_{20}Mo_{10}Ta_{10}Ti_{20}Zr_{20}$. By replacing Hf and half of Ta in the $Ta_{20}Nb_{20}Hf_{20}Zr_{20}Ti_{20}$ alloy with lighter Cr and Mo, respectively, the density of the new alloy was reduced to 8.2 g/cm^3. In addition, the new alloy showed improved high temperature strength, relative to the $Ta_{20}Nb_{20}Hf_{20}Zr_{20}Ti_{20}$ alloy, and improved room temperature ductility, relative to the $Ta_{25}Nb_{25}W_{25}Mo_{25}$, $Ta_{20}Nb_{20}W_{20}Mo_{20}V_{20}$ alloys.

2. Experimental procedures

The $Nb_{20}Cr_{20}Mo_{10}Ta_{10}Ti_{20}Zr_{20}$ (which is also called $NbCrMo_{0.5}Ta_{0.5}TiZr$) alloy was prepared by vacuum arc melting of the pure elements. Nb, Cr, Ti and Zr were taken at equal molar fractions, while the molar fractions of Mo and Ta were twice smaller. Titanium and zirconium were in the form of 3.175 mm diameter slugs with purities of 99.98% and 99.95%, respectively. Niobium, tantalum and molybdenum were in the form of 1.0, 2.0 and 4.6 mm diameter rods, and their purities were 99.95%, 99.9% and 99.0%, respectively. Chromium was in the form of 3–12 mm pieces with the purity of 99.95%. High vacuum of 2.1×10^{-4} N/m^2 was achieved in the arc melting chamber prior to filling the chamber with high purity argon at the pressure of 5.1×10^4 N/m^2. High purity molten titanium was used as a getter for residual oxygen, nitrogen and hydrogen. Arc melting of the alloy was conducted on a water-cooled copper plate. To achieve homogeneous distribution of elements, the alloy was re-melted and flipped five times, and was in a liquid state for about 5 min during each melting event. The prepared sample was about 15 mm thick, 35 mm wide and 100 mm long and had shiny surfaces. The actual alloy composition determined with the use of inductively coupled plasma-optical emission spectroscopy (ICP-OES), is given in Table 1. The crystal structure was identified with the use of a Rigaku X-ray diffractometer, Cu Kα radiation, and the 2θ range of 5–140°.

To close porosity in the as-solidified alloy, it was hot isostatically pressed (HIPd) under the following conditions. The alloy sample was placed inside a 63 mm diameter alumina can. The alumina can was inserted inside a 75 mm diameter graphite can, which was used as a heating element and located inside the HIP unit chamber. The chamber was evacuated to $\sim 1.3 \times 10^{-4}$ N/m^2, filled with high purity argon and the sample was heated at a constant rate of 10 K/min to 1723 K with a simultaneous increase in the argon pressure in the chamber to 207 MN/m^2. The sample was held at 1723 K/207 MN/m^2 for 3 h and cooled to room temperature at ~20 K/min with simultaneous pressure release.

The density of the alloy was measured with an AccuPyc 1330 V1.03 helium pycnometer. The pycnometer cell volume was 12.2284 cm^3, the weight of the sample was ~10 g and was measured with the accuracy of ±0.0001 g, and the volume of the samples was determined with the accuracy of ±0.0001 cm^3 by measuring the free volume of the loaded cell using helium gas and 10 purges. Vickers microhardness was measured on polished cross-section surfaces using a 136° Vickers diamond pyramid under 500 g load applied for 30 s. The microstructure was analyzed with the use of a scanning electron microscope (SEM) Quanta 600F (FEI, North America NanoPort, Hillsboro, Oregon, USA) equipped with a backscatter electron (BSE), energy-dispersive X-ray spectroscopy (EDS), and electron backscatter diffraction (EBSD) detectors. A step size of 0.2 μm was used for simultaneous EDS and EBSD mapping.

Cuboids-shaped specimens for compression testing were electric-discharge machined from the HIPd alloy. The specimen compression axis was perpendicular to the alloy surface, which was in contact with the copper plate during arc melting. The specimen surfaces were mechanically polished and the compression faces of the specimens were paralleled and lubricated with boron nitride (for elevated temperature tests). The specimen's dimensions were ~4.7 mm × 4.7 mm × 7.7 mm. Compression tests were conducted at temperatures 1073 K, 1273 K and 1473 K in a computer-controlled Instron (Instron, Norwood, MA) mechanical testing machine outfitted with a Brew vacuum furnace and silicon carbide dies. Prior to each test, the furnace chamber was evacuated to ~10^{-4} N/m^2. The test specimen was then heated to the test temperature at a heating rate of ~20 K/min and soaked at the temperature for 15 min under 5 N controlled load, and then compressed to a 50% height reduction or to fracture, whichever happened first. A constant ramp speed that corresponded to an initial strain rate of 10^{-3} s^{-1} was used. Room temperature testing was conducted at the same loading conditions but in air, and a thin Teflon foil was used between the compression faces and silicon carbide dies to reduce friction. The deformation of all specimens was video-recorded and an optical setup was used to measure strain vs. load.

3. Results and discussion

3.1. Crystal structure and microstructure of the as-solidified and HIPd alloy

Fig. 1 shows the X-ray diffraction patterns of the $NbCrMo_{0.5}Ta_{0.5}TiZr$ alloy in (a) as-solidified and (b) HIPd conditions. The diffraction peaks from three phases, two with the body centered cubic (BCC1 and BCC2) lattices and one with the face centered cubic (FCC, Laves C15) lattice, are easily identified in the as-solidified condition (see Fig. 1a), and the lattice parameters of these phases were determined to be $a = 325.46 \pm 0.11$ pm, 338.6 ± 0.4 pm, and 733.38 ± 0.18 pm, respectively. The HIP processing broadened the X-ray peaks from the BCC1 and FCC phases and reduced the intensities of the peaks of the BCC2 and FCC phases relative to the peak intensities of the BCC1 phase (Fig. 1b), which increased errors in the measurements of the lattice parameters of these minor phases. The lattice parameter of the BCC1 phase slightly decreased ($a = 324.76 \pm 0.16$ pm), BCC2 phase increased ($a = 341 \pm 1$ pm) and FCC phase increased ($a = 740.0 \pm 0.5$ pm) after HIP.

Microstructure of the HIPd alloy is shown in Fig. 2. Three characteristic microstructural constituents are clearly recognized on the backscatter electron (BSE) images. These are (i) large branching bright particles, (ii) a dark continuous matrix between the bright particles, and (iii) smaller dark particles precipitated inside the matrix. Additionally, an about 3 μm thick transition layer (TL) can be seen at the surfaces of the bright particles (Fig. 2b). The electron backscatter diffraction (EBSD) analysis indicated that both the bright particles and the dark matrix, as well as the transition layer, have the BCC crystal structures, while the smaller dark particles have a FCC crystal structure (Fig. 3a and b). Note that in the secondary electron (SE) image mode (Fig. 3a), the light-gray color code of the FCC particles is similar to the color code of large BCC1 particles. Although the EBSD method cannot distinguish the BCC1 and BCC2 phases, which have different lattice parameters, these phases

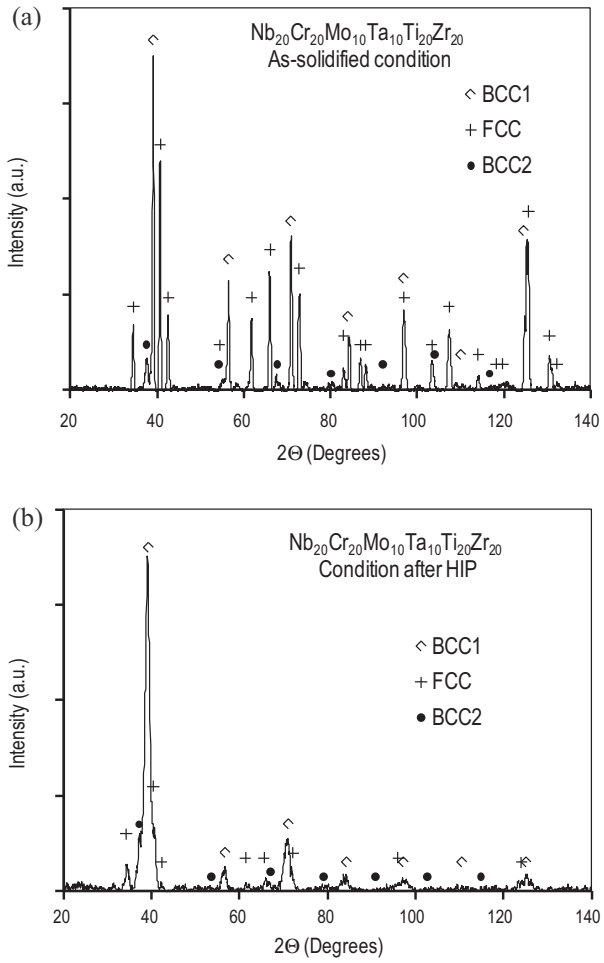

Fig. 1. X-ray diffraction patterns of the $NbCrMo_{0.5}Ta_{0.5}TiZr$ alloy in (a) as-solidified and (b) HIPd conditions. The indexed peaks belong to two BCC and one FCC crystal phases.

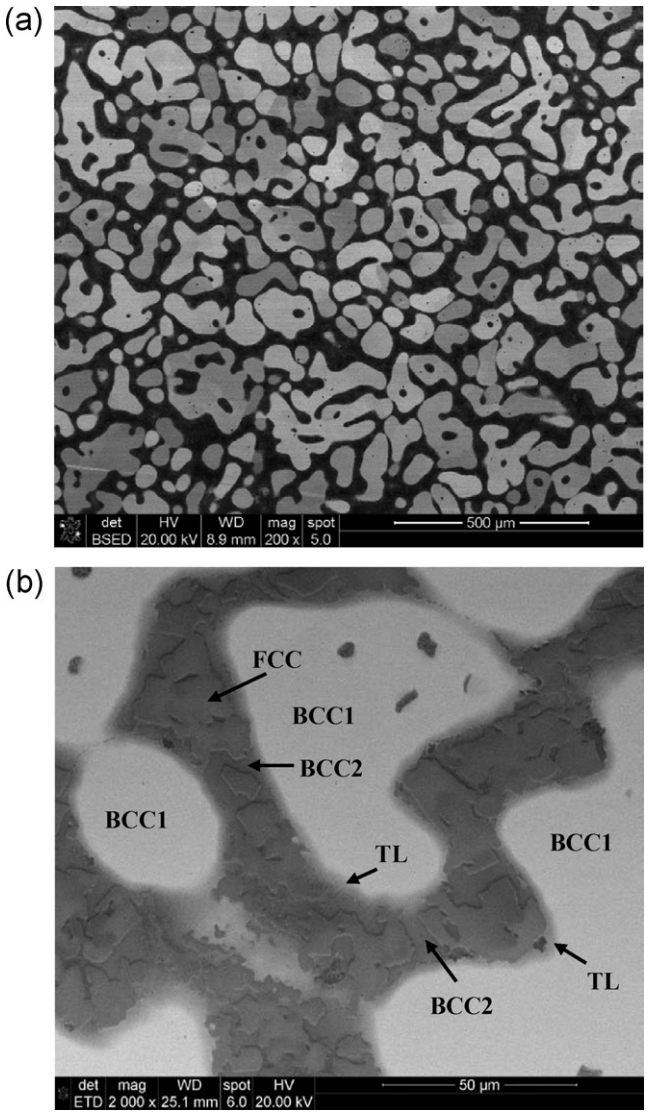

Fig. 2. SEM backscatter electron images of a polished cross-section of the HIPd $NbCrMo_{0.5}Ta_{0.5}TiZr$ alloy. The three phases (BCC1, BCC2 and FCC) with different morphologies and contrasts, as well as the transition layer (TL), are indicated.

can be identified by comparing their volume fractions. Indeed, the volume fractions of the bright particles, dark particles and the matrix were determined to be ~67%, 17% and 16%, respectively. Comparing these results with the results of the X-ray diffraction concludes that the bright particles have the BCC1 crystal structure, while the matrix phase has the BCC2 crystal structure. EDS mapping showed that these phases have different concentrations of alloying elements. For example, Fig. 3c illustrates that the concentration of Ti is much higher in the BCC2 phase than in the BCC1 phase, while the FCC phase has the lowest concentration of Ti.

Quantitative chemical analysis of these three phases was conducted with the use of an EDS detector attached to the field emission gun SEM. The results are given in Table 2. It is found that the BCC1 phase is enriched with Nb, Mo and Ta, which are the BCC forming elements, and depleted with Cr and Zr. The amount of Ti in the BCC1 phase is close to the average alloy composition. The BCC2 phase, on the other hand, is highly enriched with Ti and Zr and depleted with Cr, Mo and Ta. The amount of Nb in this phase is only slightly lower of the average alloy composition. In spite of the reduced amount of the BCC-forming elements in the BCC2 phase, their total concentration is still high, ~26 at.%, thus stabilizing the high-temperature polymorph of the Ti and Zr rich phase. The FCC phase contains an increased amount of Cr (~41 at.%) and reduced amounts of Mo, Nb, Ta and Ti. This Laves phase can be described by a formula $(Zr,Ta)(Cr,Mo,Nb)_2$, with Ti equally substituting both larger and smaller elements. Finally, the transition layer at the surface of the BCC1 particles has a reduced concentration of Cr and Mo and an increased concentration of Ti and Zr, relative to the composition of the interior part of these particles. The chemical composition of this layer is very different from the compositions of two other phases, BCC2 and FCC. Therefore, one may suggest that this layer retains the BCC1 crystal structure of the underneath particles.

It is interesting to note that the inverse pole figure (IPF) maps from the BCC and FCC phases, Fig. 3(d–f) show that the BCC2 matrix grains have the same crystallographic orientations as the adjacent BCC1 particles. On the other hand, no correlation between the crystallographic orientations of the BCC2 matrix and FCC particles was identified. This result may indicate that the BCC1 and BCC2 phases originate from the same high-temperature single BCC phase, i.e. just below the melting temperature the alloy has a single-phase BCC crystal structure. During cooling, this high-temperature BCC phase rejects Cr and Zr into the grain boundaries. Subsequently, the Cr and Zr enriched grain boundary regions experience the phase transformation resulting in formation of the Cr-rich FCC particles (Laves phase) and Zr- and Ti-rich continuous BCC2 phase. According to this scenario, the discontinuous BCC1 particles should be considered as the remaining high-temperature matrix phase and the continuous BCC2 phase as a secondary phase formed along the

Table 2
Chemical composition (in at.%) of different microstructure constituents in the HIPd $NbCrMo_{0.5}Ta_{0.5}TiZr$ alloy.

Constituent	Phase	Nb	Cr	Mo	Ta	Ti	Zr
4 mm^2 area	BCC1 + BCC2 + FCC	22.20	18.35	10.15	11.73	19.30	18.27
Primary bright particles	BCC1	26.80	13.22	14.30	16.80	19.07	9.82
Matrix between the primary particles	BCC2	18.68	3.09	0.64	3.83	33.16	40.60
Dark particles inside the matrix	FCC (Laves)	12.07	40.74	6.35	6.99	10.78	23.09
Transition layer	BCC1	26.96	6.74	9.92	14.14	28.08	14.16

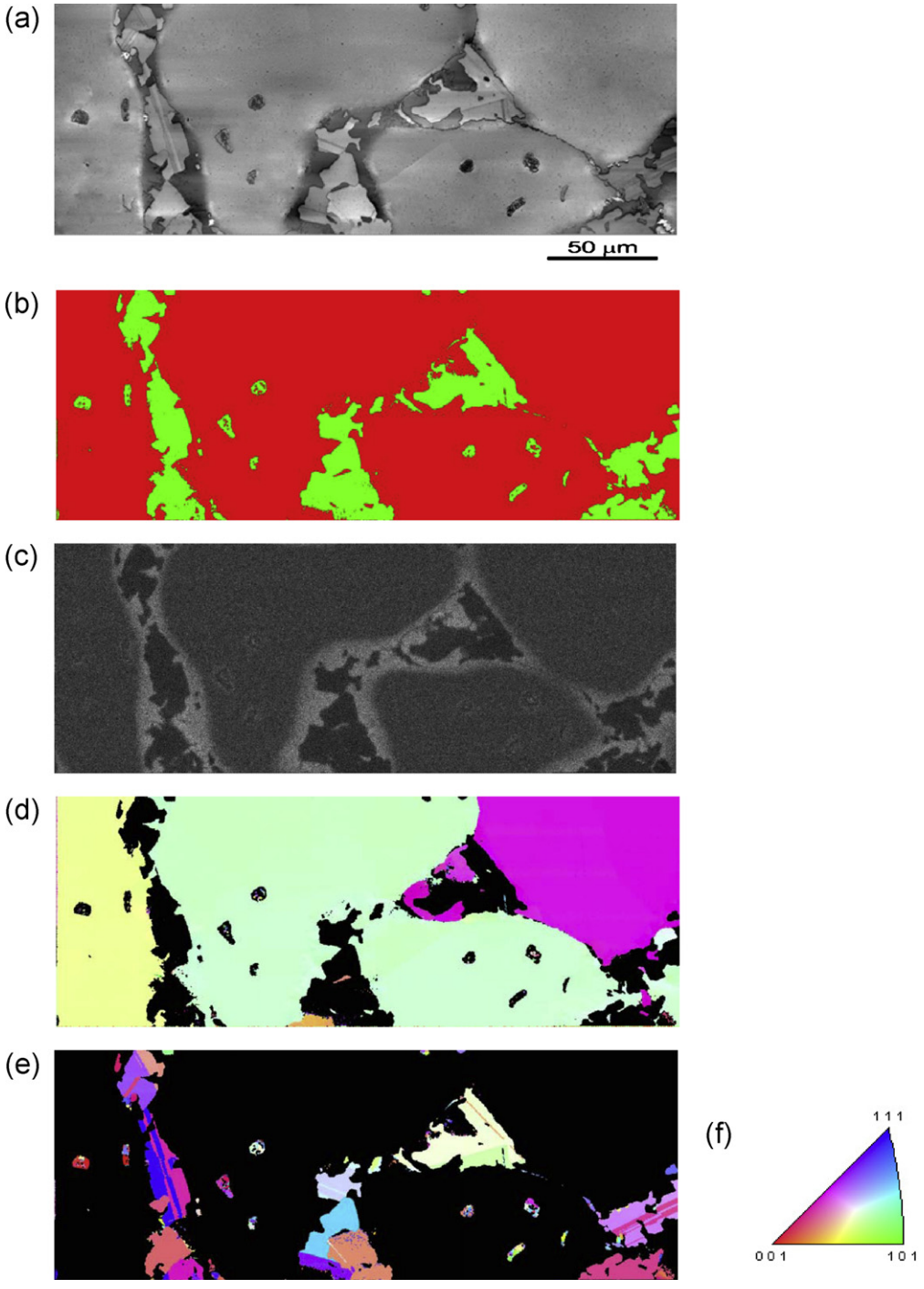

Fig. 3. (a) Secondary electron (SE) image, (b) phase map, (c) EDS map of Ti, and (d and e) inverse pole figure (IPF) maps of (d) the BCC and (e) FCC phases. In (b), the BCC phases are colored by red and the FCC phase is colored by green. In (c), the lighter regions are enriched and darker regions are depleted with Ti. The crystallographic orientations of different grains in (d) and (e) are identified by the color scheme in the IPF triangle (f). (For interpretation of the references to color in this figure legend, the reader is referred to the web version of the article.)

Table 3
The lattice parameter, a, of the BCC crystal structure of the pure metals and the BCC1 and BCC2 phases presented in the studied alloy at room temperature. For Zr and Ti, the parameter a was extrapolated from elevated temperatures [8]. The calculated (Calc) values of the lattice parameter of the BCC phases were obtained using Eq. (1).

	Metal									
	Nb	Cr	Mo	Ta	Ti	Zr	BCC1 Calc	BCC2 Calc	BCC1 HIP	BCC2 HIP
a (pm)	330.1	288.4	315.0	330.3	327.6	358.2	324.7	339.3	324.8	341.0

Table 4
Density of pure metals and the studied $NbCrMo_{0.5}Ta_{0.5}TiZr$ alloy. Both calculated (Calc, using Eq. (2)) and experimental (Exp) values are shown for the alloy.

	Metal								
	Nb	Cr	Mo	Ta	Ti	Zr	Alloy (Calc)	Alloy Cast (Exp)	Alloy HIP (Exp)
ρ (g/cm^3)	8.57	7.14	10.28	16.65	4.51	6.51	8.23	8.02	8.23

Table 5
Vickers microhardness, H_v, values of pure metals and the $NbCrMo_{0.5}Ta_{0.5}TiZr$ alloy at room temperature. Both the calculated (Calc) and experimental (Exp) values are shown for the alloy.

	Metal							
	Nb	Cr	Mo	Ta	Ti	Zr	Alloy (Calc)	Alloy (Exp)
H_v (MPa)	1320	1060	1530	873	970	903	1097	5288

grain boundaries of the high-temperature BCC1 phase as a result of the solid-state phase transformation. Additional work is required for studying solid-state reactions in this alloy.

Using the rule of mixtures (i.e. Vegard's law [13]) and known concentrations of the alloying elements in the BCC1 and BCC2 phases, one can calculate the crystal lattice parameter a_{mix} of the respective disordered BCC solid solutions:

$$a_{mix} = \sum c_i a_i \quad (1)$$

Here c_i is the atomic fraction of element i and a_i is the lattice parameter of the BCC crystal lattice of element i at room temperature. The calculated (Calc) a_{mix} are given in Table 3 along with the experimental (Exp) a values determined from the X-ray diffraction. The calculated and experimental values of a for the BCC1 phase are practically the same; however, the experimental value of a for the BCC2 phase in the HIPd alloy is about 0.5% higher than the respective calculated value. This discrepancy can be due to a large experimental error in determining a from low-intensity X-ray diffraction peaks of the BCC2 phase. The same calculated and experimental values of the lattice parameter suggest that the alloying elements are randomly distributed in the BCC phases.

3.2. Density and microhardness

The density of the alloy in the as-solidified and HIPd conditions was determined to be $\rho = 8.02 \pm 0.01$ g/cm^3 and 8.23 ± 0.01 g/cm^3, respectively. A 2.6% increase in the alloy density after HIPing is probably due to closing the same volume fraction (~2.6%) of the porosity, which was eventually present in the as-solidified material. Using the densities of pure elements (Table 4) and the alloy composition (Table 1), one can estimate the density, ρ_{mix}, of a disordered solid solution of the same composition using the rule of mixtures:

$$\rho_{mix} = \frac{\sum c_i A_i}{\sum c_i A_i / \rho_i} \quad (2)$$

Here A_i and ρ_i are the atomic weight and density of element i. Thus calculated ρ_{mix} value is 8.23 g/cm^3, which is exactly the same as the density of HIPd alloy. The fact that the average alloy density follows the rule of mixtures of pure elements, in spite of the alloy contains 2 disordered BCC phases with the total volume fraction of 83% and one ordered FCC phase with the volume fraction of 17%, may indicate that the decomposition of the high-temperature single BCC phase into these three phases did not affect the average coefficient of thermal expansion and, thus, density of the alloy at room temperature.

Table 6
Compression yield strength, $\sigma_{0.2}$, peak stress, ε_p, and fracture strain, ε_f, of the $NbCrMo_{0.5}Ta_{0.5}TiZr$ alloy at different temperatures. The strain, ε_f, rate is 10^{-3} s^{-1}.

	T (K)			
	296	1073	1273	1473
$\sigma_{0.2}$ (MPa)	1595	983	546	170
σ_p (MPa)	2046	1100	630	190
ε_f (%)	5.0	5.5	No fracture	No fracture

Vickers microhardness H_v of the HIPd alloy was measured in twenty randomly selected locations and the average value was 5288 MPa. The scatter around the average microhardness value was $\Delta H_v = \pm 71$ MPa. The microhardness of the alloy does not follow the rule of mixtures of the respective properties of the constituent elements. Indeed, Table 5 shows typical H_v [14] values for pure elements at room temperature. Using the rule of mixtures, the microhardness, $(H_v)_{mix} = \sum c_i H_{Vi}$, was calculated to be $(H_v)_{mix} = 1097$ MPa. This value is much smaller than the experimental H_v value. The high microhardness of the alloy is likely originated from the combination of precipitation and solid solution-like strengthening.

3.3. Compression properties and microstructure of deformed alloy

3.3.1. Compression properties

The engineering stress, σ, vs. engineering strain, ε, curves of the $NbCrMo_{0.5}Ta_{0.5}TiZr$ alloy obtained during compression testing at different temperatures are shown in Fig. 4. The yield strength values, $\sigma_{0.2}$, at $\varepsilon_p = 0.2\%$, where ε_p is the engineering plastic strain, peaks strength, σ_p, and fracture strain, ε_f, are given in Table 6. During deformation at 296 K, the yield strength was 1595 MPa and continuous strengthening occurred until the alloy fractured by localized shear at the peak strength of 2046 MPa accumulating about 5% strain. During testing at $T = 1073$ K, $\sigma_{0.2}$ decreased to 983 MPa, the peak strength of 1100 MPa was achieved at 4.2% strain and the sample fractured by shear at about 5.5–6% strain, after a decrease in strength to 1050 MPa. An increase in the testing temperature to 1273 K resulted in a considerable softening of the

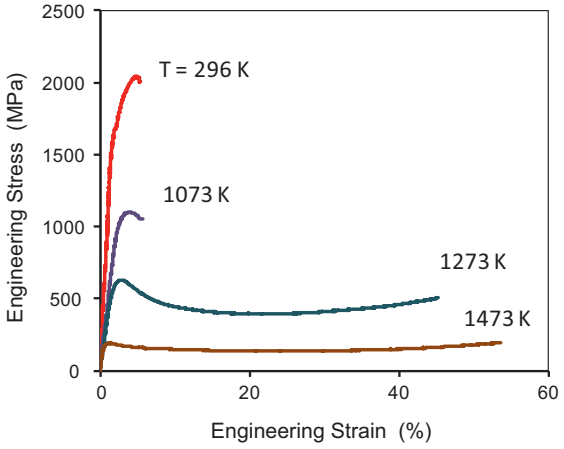

Fig. 4. The engineering stress vs. engineering strain compression curves of HIPd $NbCrMo_{0.5}Ta_{0.5}TiZr$ alloy samples at 296 K, 1073 K, 1273 K, and 1473 K.

alloy after a short stage of strain hardening. At this temperature, $\sigma_{0.2}$ = 546 MPa, σ_p = 630 MPa and the minimum strength achieved during strain softening was 393 MPa after about 22% plastic strain. At this temperature, the sample did not fracture. An increase in the temperature to 1473 K, led to further decrease in the flow stress of the alloy and $\sigma_{0.2}$ was 170 MPa. The peak stress of 190 MPa was reached shortly after yielding and followed by weak softening and a steady state flow at σ_{min} = 135 MPa. No sample fracture occurred at this temperature.

3.3.2. *Microstructure of deformed samples*

Typical microstructure features of the fracture surface of the alloy sample deformed at room temperature are shown in Fig. 5. A mixture of ductile and brittle fracture can be seen at low magnification in Fig. 5a. The ductile fracture leads to formation of dimples of different sizes and morphology (Fig. 5(b,c)), while the brittle fracture occurs by quazi-cleavage of the FCC (Laves) phase, as well as along the interfaces (Fig. 5(a and d)).

The brittle behavior of the Laves phase also led to low ductility at 1073 K. Fracture at this temperature occurred along the boundaries between the BCC2 and Laves phases (Fig. 6(a–d)); however, few cracks propagated inside the large BCC1 particles can also be seen in Fig. 6a and b. Fine (secondary) BCC1 nano-particles precipitated near the original (primary) large BCC1 particles inside the BCC2 phase are shown in Fig. 6d. Their size rapidly decreases with an increase in the distance from the primary BCC1 particle, with which the small particles are associated. These secondary BCC1 nano-particles were not observed in non-deformed sample. It is likely that at 1073 K the solubility of Nb, Mo and Ta in the BCC2 phase is considerably higher than at room temperature and the plastic deformation accelerates diffusion of the heavy elements from the primary BCC1 particle into the adjacent BCC2 matrix leading to partial dissolution of the BCC1 phase. The concentration of Nb, Mo and Ta is thus the highest near the primary particle interface and exponentially decreases with an increase in the distance from the interface. Upon cooling after testing, re-precipitation of the BCC1 phase occurs. Due to a strong temperature dependence of the solubility, the precipitation in the regions with higher concentration of the elements occurs at higher temperatures. This leads to formation of larger secondary particles near the primary BCC1 particles and smaller particles at larger distances. Knowing the width of the region, l, where the precipitation occurred ($l \sim 6\,\mu m$) and the time of the specimen holding at 1073 K ($t \sim 1000s$) the effective diffusion coefficient, D_{eff}, of these elements in the BCC2 phase during compression at 1073 K can be estimated as $D_{eff} = l^2/(2t) \approx 1.8 \times 10^{-10}\ cm^2/s$. This estimated value is about one

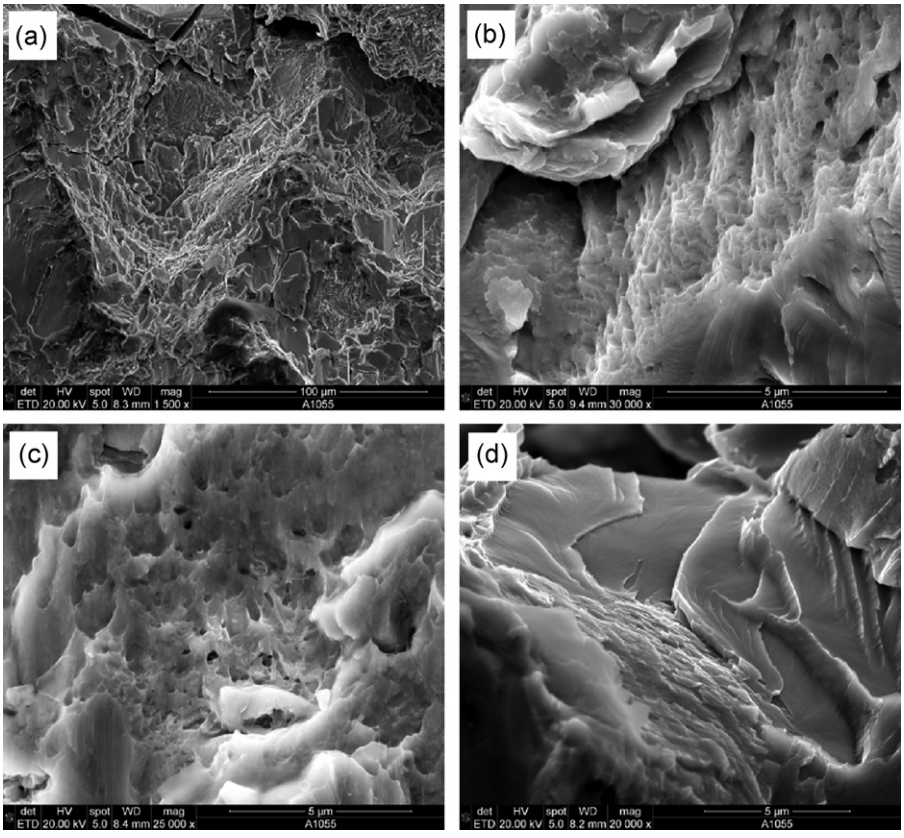

Fig. 5. SEM secondary electron images of the fracture surface of an $NbCrMo_{0.5}Ta_{0.5}TiZr$ alloy samples after compression deformation at room temperature.

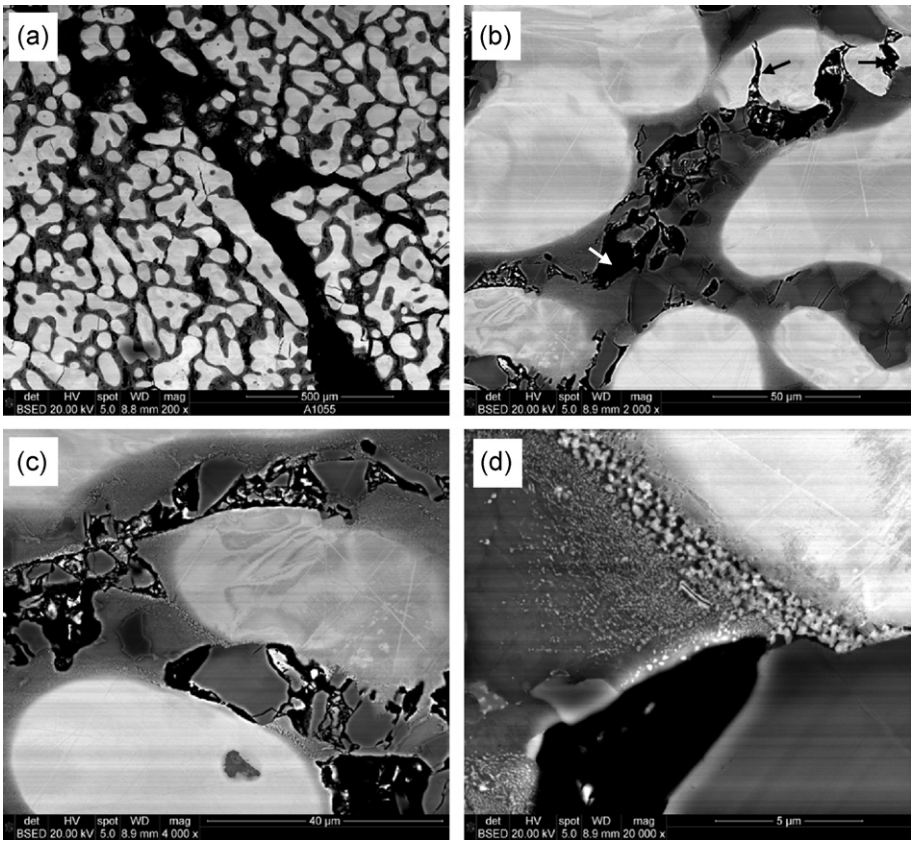

Fig. 6. SEM backscatter images of the microstructure of an $NbCrMo_{0.5}Ta_{0.5}TiZr$ alloy sample after compression deformation at 1073 K. Black regions in the figures are open cracks and three characteristic cracks are indicated by arrows in (b). The compression direction is vertical.

order of magnitude higher than the reported diffusion coefficient of Nb at the same temperature in BCC Zr–Nb alloys [15] and more than 5 orders of magnitude higher than the reported self-diffusion coefficient of Nb [16]. However, the diffusivity of elements is known to considerably increase during plastic deformation [17]. It is necessary to point out that these secondary BCC1 nano-particles replace and extend the transition layer, which is present at the surfaces of the primary BCC1 particles in non-deformed samples (Fig. 2). It is likely that the plastic deformation at 1073 K accelerates dissolution of this layer in the adjacent BCC2 matrix and re-precipitation of the BCC1 nano-particles during the following cooling.

A representative microstructure of the HIPd alloy after 50% compression at 1273 K is shown in Fig. 7. The primary BCC1 particles are compressed in the loading direction (Fig. 7a). No cracks or porosity are detected. Fine equiaxed secondary BCC1 particles precipitate inside the BCC2 matrix near the surfaces of the primary BCC1 particles, while the transition layer disappears, similar to the situation observed in the sample deformed at 1073 K. However, these fine particles are coarser after deformation at 1273 K (compare Fig. 7b and Fig. 6d), their average size is estimated to be ~0.7–0.8 μm, and no noticeable decrease in the secondary particle size is seen with an increase in the distance from the associated primary particle. In addition, many of these secondary particles are aligned in chains oriented about 45–65° to the compression direction and form characteristic tails at the respective primary particles (two tails are indicated by arrows in Fig. 7c). Directions of these aligned chains of fine particle are likely associated with the directions of the local shear propagation. A round primary BCC1 particle sheared at about 45° to the compression direction is also seen in Fig. 7a, and it is shown in Fig. 7c at a higher magnification. On the opposite sides of this particle there are two tails of fine particles, which are oriented in slightly different directions. These observations indicate that the local plastic flow changes orientation in the deformed alloy sample within ~100 μm scale. They also indicate that the fine secondary BCC1 particles were formed during deformation and then moved away from the primary BCC1 particles due to localized plastic flow, or the regions of the BCC2 matrix, which were adjacent to the large BCC1 particles and enriched with Nb, Mo and Ta, were heavily deformed and moved away from the particle interfaces at 1273 K, but the fine particles were formed inside these regions during cooling due to the temperature-dependent solubility. Additional work is required to identify the correct scenario of formation of the aligned chains of fine BCC1 particles. Fine, nanometer-size precipitates of the Laves phase are observed inside the primary BCC1 particles in the deformed sample (Fig. 7d). These precipitates are coarser at grain boundaries (Fig. 7d).

To separate two effects, temperature and deformation, on the microstructure evolution, the microstructure of an non-deformed sample that, identically to the deformed sample, was heated to 1273 K, held at this temperature for 1460 s and cooled down to room temperature, was studied, and it is shown in Fig. 8. The microstructure of this sample looks similar to the microstructure of the HIPd sample (compare Fig. 2 and Fig. 8a). Annealing at 1273 K for 1460 s did not dissolve the transition layer (TL) at the surfaces of the primary BCC1 particles. However, a higher magnification image (Fig. 8b) shows that the decomposition of this TL has just started and few secondary BCC1 particles are spotted adjacent to this layer. Nanometer-sized precipitates are observed inside the primary BCC1 particles (Fig. 8b); however, their size is much smaller than in the deformed sample (Fig. 7d). This comparison of the microstructure of the deformed and non-deformed samples clearly indicates that the plastic deformation accelerates diffusion-related processes, such as phase transformations and particle coarsening.

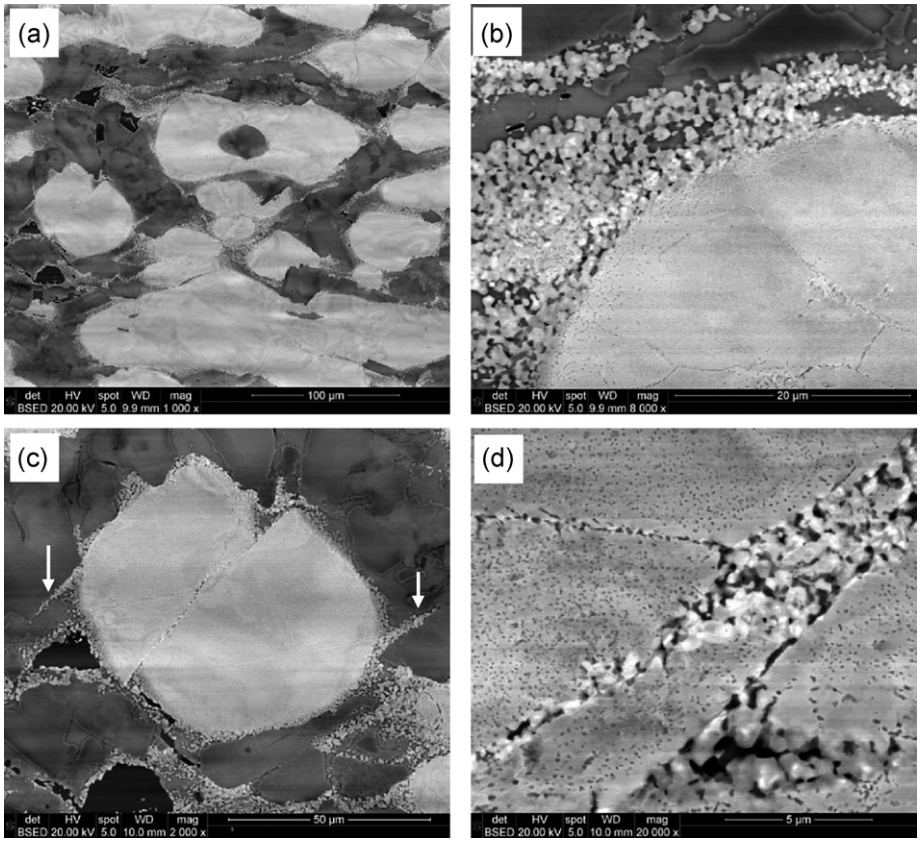

Fig. 7. SEM backscatter images of the microstructure of an $NbCrMo_{0.5}Ta_{0.5}TiZr$ alloy sample after compression deformation at 1273 K. Two characteristic tails consisting of nano-particles are indicated by arrows in (c). The compression direction is vertical.

Fig. 9 illustrates the microstructure of the HIPd alloy after 50% compression at 1473 K. Many primary BCC1 particles become elongated and some are severely deformed in the directions of plastic flow of the material (Fig. 9a). Similar to deformation at 1273 K, these particles have characteristic tails oriented in the directions of local plastic flow (some of these tails are indicated by arrows in Fig. 9a and c). However, while at 1273 K these tails consist of fine separated secondary BCC1 particles embedded in the BCC2 phase, at 1473 K the tails consist of larger size (~2–3 μm) coalesced BCC1 particles (see Fig. 9c). Deformation of the BCC2 matrix results in recrystallization and formation of equiaxed grains (Fig. 9d). At the same time, the FCC (Laves) particles embedded in the BCC2 matrix remain practically non-deformed and still impede the plastic flow, as it is clearly seen in Fig. 9b. Twins, observed inside some FCC particles, are probably annealing twins as they are also present in non-deformed samples. Fine precipitates observed inside the primary BCC1 particles become clearly visible due to coarsening. These precipitates decorate grain boundaries, but they are also present inside the grains (see Fig. 9). The EBSD analysis indicates that these precipitates have the FCC crystal structure (Fig. 10) and are likely the Laves phase.

The results of the EDS analysis of different microstructural constituents presented in the sample after compression at 1473 K are given in Table 7. The average composition of the sample, measured from the area of ~6 mm^2, is almost the same as the average composition of the as-solidified (Table 1) and HIPd (Table 2) samples.

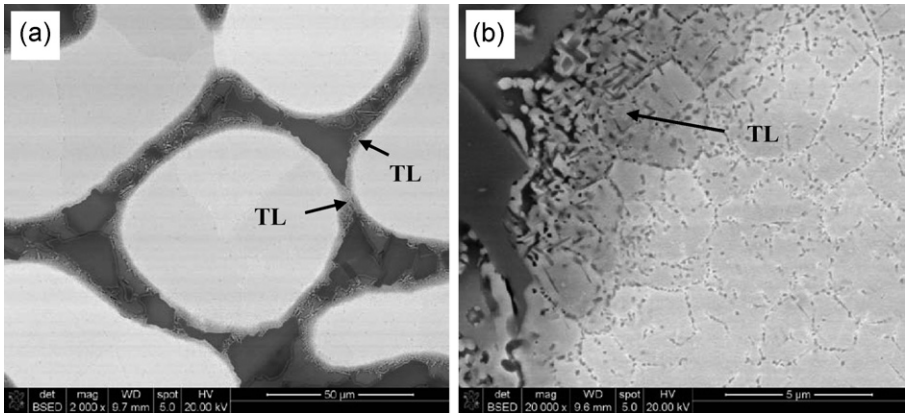

Fig. 8. SEM backscatter images of the microstructure of an $NbCrMo_{0.5}Ta_{0.5}TiZr$ alloy sample after holding at 1273 K for 1460 s. The sample experienced the same heating and cooling conditions as the sample plastically compressed by 50% at 1273 K (see Fig. 7.). Transition layers (TL) at surfaces of BCC1 particles are indicated by arrows.

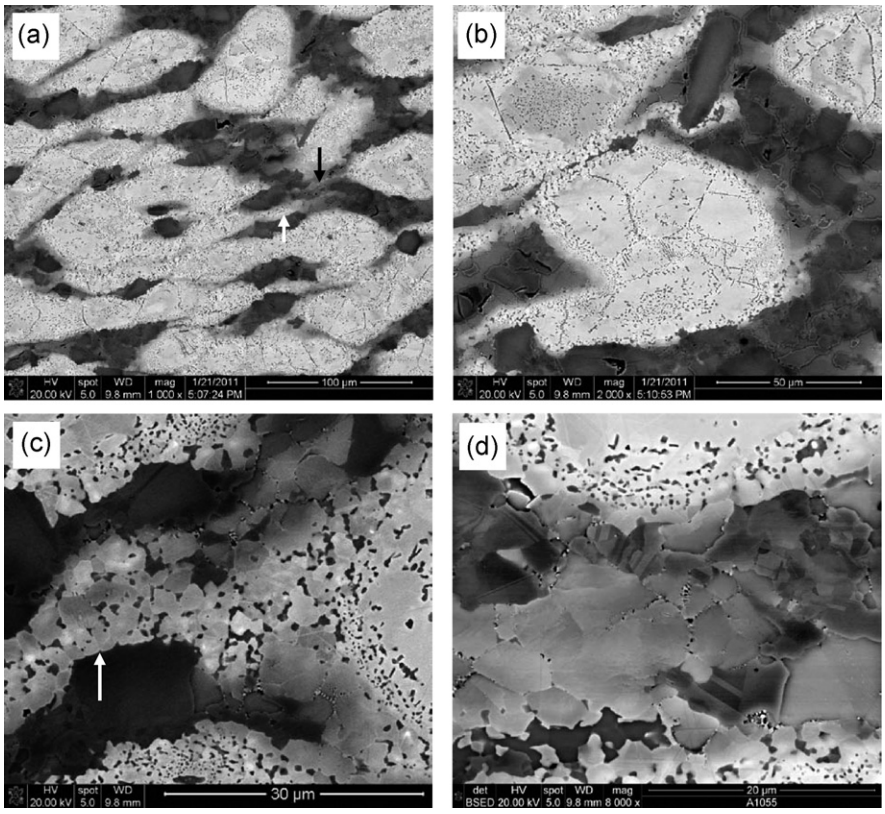

Fig. 9. SEM backscatter images of the microstructure of an $NbCrMo_{0.5}Ta_{0.5}TiZr$ alloy sample after compression deformation at 1473 K. Several characteristic tails at deformed BCC1 particles are indicated by arrows. The compression direction is vertical.

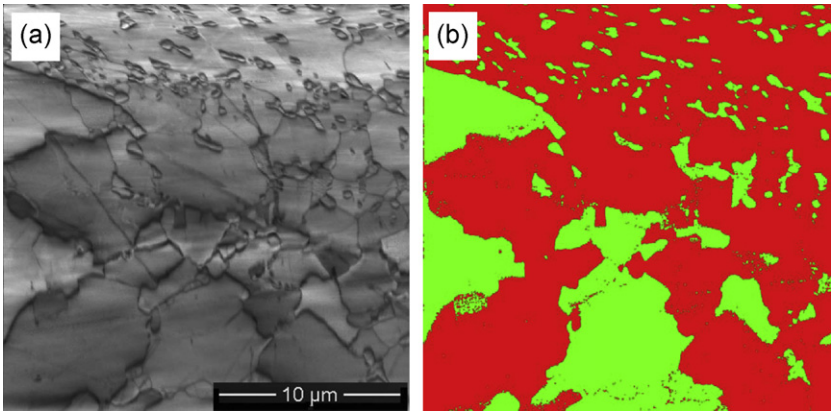

Fig. 10. (a) SEM secondary electron image of the microstructure of an $NbCrMo_{0.5}Ta_{0.5}TiZr$ alloy sample after compression at 1473 K and (b) respective phase map. The BCC phases are red and the FCC (Laves) phase is green. (For interpretation of the references to color in this figure legend, the reader is referred to the web version of the article.)

Table 7
Chemical composition (in at.%) by EDS/SEM of different constituents in the $NbCrMo_{0.5}Ta_{0.5}TiZr$ alloy sample after 50% compression at 1473 K.

Constituent	Phase	Nb	Cr	Mo	Ta	Ti	Zr
6.0 mm^2 area	BCC1 + BCC2 + FCC	22.20	18.39	10.07	11.78	19.36	18.20
Primary bright particles	BCC1 + FCC	26.93	13.29	13.76	16.06	19.38	10.57
Bright region inside primary particles	BCC1	27.62	11.53	13.97	16.29	20.06	10.53
Dark precipitates inside primary particles	FCC (Laves)	17.91	30.30	11.19	11.19	13.30	16.12
Dark matrix between primary particles	BCC2	20.35	2.54	1.23	4.57	31.41	39.90
Dark particles inside the matrix	FCC (Laves)	11.90	41.06	6.74	7.11	10.48	22.71
Bright particles inside the tails	BCC1	27.59	6.80	8.27	12.90	28.01	16.44

Because these samples were randomly extracted from different regions of the arc-molten ingot, this result indicates no macrosegregation of elements in the ingot. Comparison of the concentrations of the alloying elements in different phases of the deformed and HIPd samples shows that, after compression at 1473 K, the BCC2 phase becomes slightly enriched with Nb, Mo and Ta and depleted with Ti, Zr and Cr, while the FCC phase becomes slightly enriched with Mo and Cr and depleted with Zr. The composition of the primary BCC1-rich particles also slightly changes due to a slight (~0.75 at.%) increase in Zr and the same decrease in Ta. These particles in the deformed sample consist of two phases: major BCC1 and minor FCC (Laves), the latter is in the form of nano-precipitates (Fig. 9). Because the precipitates are enriched with Cr, the remaining BCC1 phase is slightly depleted with this element (see Table 7). The small bright particles inside the tails (see Fig. 9c), although they have the BCC1 crystal structure, have increased amounts of Zr and Ti and reduced amounts of Cr, Mo and Ta relative to the BCC1 phase of the large primary particles. The composition of these particles is close to the composition of the transition layer at the surfaces of the primary BCC1 particles in the non-deformed alloy (see Table 2). This result supports our earlier conclusion that these tail particles precipitate inside the transition regions between the primary BCC1 particles and the BCC2 matrix during or after deformation.

The microstructural analysis results clearly indicate that the microstructure of the as-solidified and HIPd at 1723 K alloy is metastable and it experiences phase and structural transformations during the following heating to the temperature range of 1073–1473 K. Namely, nano-precipitation and coarsening of secondary BCC1 particles inside the BCC2 phase and FCC particles inside the primary BCC1 particles occur in this temperature range. Plastic deformation increases the rate of these transformations by several orders of magnitude, probably by creating high number density of excess vacancies [17].

4. Conclusions

A new refractory alloy, $NbCrMo_{0.5}Ta_{0.5}Ti_{20}Zr_{20}$, was produced and its crystal structure, microstructure, density, hardness and compression properties were determined in the as-solidified and HIPd condition. The alloy consisted of two disordered BCC1 and BCC2 phases and one ordered FCC (Laves C15) phase. After HIP at 1723 K, 207 MPa for 3 h, the BCC1 phase was present in the form of large individual particles, which were surrounded by the BCC2 phase. Smaller particles of the Laves phase were present inside the BCC2 phase. The volume fractions of the BCC1, BCC2 and FCC phases were 67%, 16% and 17%, respectively. The HIPd alloy density was $\rho = 8.23\ g/cm^3$ and the Vickers microhardness was $H_v = 5.29$ GPa. The alloy showed high yield strengths of $\sigma_{0.2} = 1595$ MPa, 983 MPa, 546 MPa, and 170 MPa at 293 K, 1073 K, 1273 K and 1473 K, respectively. Ductile type fracture occurred after ~5–6% compression strain at 293 K and 1073 K. Brittle Laves particles were responsible for the fracture at these temperatures. No fracture occurred during compression testing at 1273 K and 1473 K.

Acknowledgements

Discussions with Drs. D.M. Dimiduk, F. Meisenkothen, D.B. Miracle, T.A. Parthasarathy, A.A. Salem, G.B. Viswanathan, and G.B. Wilks are recognized. Technical help from T.A. Goff (arc melting), J.M. Scott (mechanical testing) and S.V. Senkova (SEM) is acknowledged. This work was supported through the Air Force Office of Scientific Research (Dr. Ali Sayir, Program Manager) and through the USAF Contract No. FA8650-10-D-5226.

References

[1] D.M. Dimiduk, J.H. Perepezko, MRS Bull. 28 (2003) 639–645.
[2] R.A. MacKay, T.P. Gabb, J.L. Smialek, M.V. Nathal, Alloy Design Challenge: Development of Low Density Superalloys for Turbine Blade Applications, NASA/TM, 2009, 215819.
[3] P.R. Subramanian, M.G. Mendiratta, D.M. Dimiduk, M.A. Stucke, Mater. Sci. Eng. A 2390240 (1997) 1–13.
[4] B.P. Bewlay, M.R. Jackson, J.-C. Zhao, P.R. Subramanian, Metall. Mater. Trans. A 34A (2003) 2043–2052.
[5] J.H. Perepezko, Science 326 (5956) (2009) 1068–1069.
[6] O.N. Senkov, G.B. Wilks, D.B. Miracle, C.P. Chuang, P.K. Liaw, Intermetallics 18 (2010) 1758–1765.
[7] O.N. Senkov, G.B. Wilks, J.M. Scott, D.B. Miracle, Intermetallics 19 (2011) 698–706.
[8] O.N. Senkov, J.M. Scott, S.V. Senkova, D.B. Miracle, C.F. Woodward, J. Alloys Compd. 509 (2011) 6043–6048.
[9] O.N. Senkov, J.M. Scott, S.V. Senkova, D.B. Miracle, C.F. Woodward, Microstructure and properties of a refractory TaNbHfZrTi alloy, Unpublished paper, 2011.
[10] J.-W. Yeh, S.-K. Chen, S.-J. Lin, J.-Y. Gan, T.-S. Chin, T.-T. Shun, C.-H. Tsau, S.-Y. Chang, Adv. Eng. Mater. 6 (5) (2004) 299–303.
[11] J.-W. Yeh, Ann. Chim.: Sci. Mater. 31 (2006) 633–648.
[12] J.-W. Yeh, Y.-L. Chen, S.-J. Lin, S.-K. Chen, Mater. Sci. Forum 560 (2007) 1–9.
[13] L. Vegard, Z. Phys. 5 (1921) 17–26.
[14] Hardnesses of the Elements, http://en.wikipedia.org/wiki/Hardnesses_of_the_elements_(data_page).
[15] Chr. Herzig, U. Kohler, S.V. Divinski, J. Appl. Phys. 85 (1999) 8119–8130.
[16] R.E. Einziger, J.N. Mundy, H.A. Hoff, Phys. Rev. B 17 (1978) 440–448.
[17] O.N. Senkov, M.M. Myshlyaev, Acta Metall. 34 (1986) 97–106.